PAPER • OPEN ACCESS

Compensation of 1/1 and 2/2 error field in Wendelstein 7-X via divertor heat load symmetrization

To cite this article: Yu Gao *et al* 2026 *Nucl. Fusion* **66** 076015

OPEN ACCESS
IOP Publishing | International Atomic Energy Agency Nuclear Fusion
Nucl. Fusion 66 (2026) 076015 (12pp) https://doi.org/10.1088/1741-4326/ae738e

Compensation of 1/1 and 2/2 error field in Wendelstein 7-X via divertor heat load symmetrization

Yu Gao[1,*], Sergey Bozhenkov[1], Yuhe Feng[1], Sebastian Thiede[1], Marcin W. Jakubowski[1], Joachim Geiger[1], Torsten Stange[1], Olaf Grulke[1], Michael Endler[1], Matthias Otte[1], Dirk Naujoks[1], Joris Fellinger[1], Fabio Pisano[2] and the W7-X Team[a]

[1] Max-Planck-Institut für Plasmaphysik, 17491 Greifswald, Germany
[2] Department of Electrical and Electronic Engineering, University of Cagliari, 09123 Cagliari, Italy

E-mail: yu.gao@ipp.mpg.de

Received 27 February 2026, revised 13 May 2026
Accepted for publication 27 May 2026
Published 9 June 2026

Abstract

Recent experiments with the water-cooled, high-heat-flux divertor of the Wendelstein 7-X (W7-X) stellarator demonstrate substantial progress in error-field compensation. Numerical simulations reveal a pronounced sensitivity of divertor heat load distributions to error fields. Experimentally, wide-angle infrared cameras monitoring all ten divertor units show significant improvements in the symmetry of divertor thermal footprints when trim coils and control coils are employed to compensate intrinsic 1/1 and 2/2 error fields, respectively. The experimentally determined amplitude of the intrinsic 1/1 error field is consistent with results obtained seven years ago, despite different diagnostics, divertor components, and slight variation in magnetic configurations. For the first time, the intrinsic 2/2 error field has been compensated through a phase-scan experiment using control coil currents, supported and validated by simulations.

Keywords: W7-X, error field, divertor, heat load

(Some figures may appear in colour only in the online journal)

1. Introduction

One of the central challenges for future fusion reactors is the management of power exhaust. Wendelstein 7-X (W7-X) [1–3], the world's most advanced stellarator, is the first device to employ an actively cooled island divertor and is among the few long-pulse magnetic confinement devices capable of sustaining high heat fluxes [4]. The intrinsic three-dimensional (3D) magnetic island structure at the plasma boundary in W7-X produces non-axisymmetric heat deposition across the ten divertor units. Although the magnetic coil system provides substantial flexibility in shaping the edge magnetic topology [5], further modifications to the thermal footprint arise from finite error fields [6, 7], toroidal plasma currents [8], plasma beta effects [9], and particle drifts [10]. Furthermore, heat transport has also been observed in geometrically shadowed divertor regions [11].

For safe plasma operation, real-time monitoring of all ten divertor units is essential. This is achieved using infrared thermographic systems [12, 13] equipped with wide-angle optics. The temperature evolution measured on the divertor target surface is processed with the newly developed DELVER code (Divertor Energy Load Versatile EstimatoR) [14], a 3D implicit anisotropic heat diffusion solver capable of handling

[a] See Grulke *et al* 2024 (https://doi.org/10.1088/1741-4326/ad2f4d) for the W7-X Team.
[*] Author to whom any correspondence should be addressed.

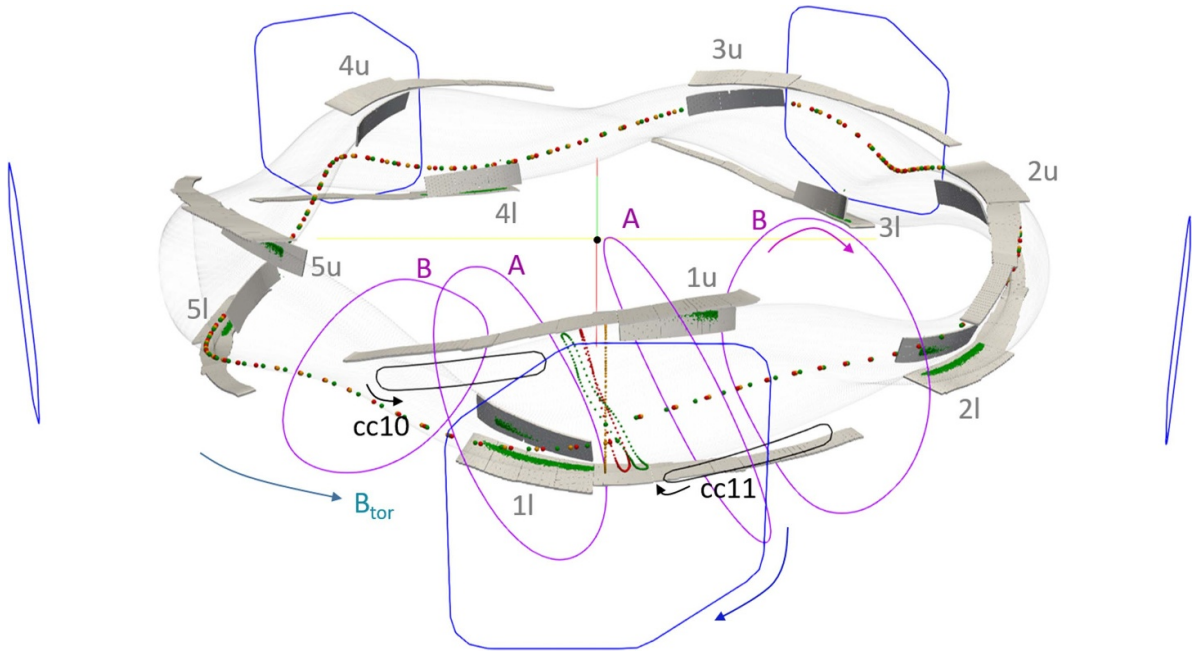

Figure 1. Overview of the ten divertor units and the coil system in W7-X, except the non-planar coils. Each divertor unit comprises one horizontal and one vertical target and is labeled 1–5 for the upper (u) and lower (l) halves of the device. Four planar coils of types A and B in module 1 are shown in purple, and two control coils (cc10 and cc11) in the same module are shown in black. These coils respect the five-fold machine symmetry, though only those in module 1 are displayed for clarity. The five trim coils are indicated in blue. Positive current directions are denoted by colored arrows. The geometric toroidal angle $\varphi_g = 0^\circ$ is defined at the center of module 1, with the positive toroidal field directed counter-clockwise when viewed from above. The $\varphi = 0^\circ$ plane and representative field lines in Boozer, Hamada, and PEST flux coordinates are plotted in red, green, and orange, respectively. The global Cartesian origin of W7-X is marked as a black dot at the figure center.

heat transport across multiple material layers, including the carbon-fiber composite, interlayers, and heat sink. DELVER also incorporates water-cooling conditions at the base and includes surface layer adjustments [15] at the top.

W7-X is designed with a five-fold toroidal modular and an up-down flip symmetry. The ten divertor units are arranged toroidally, with five in the upper half and five in the lower half of the machine (figure 1). Ideally, heat loads would be equally distributed among the ten units; however, asymmetries arise mainly due to magnetic error fields, particle drifts, and finite target-positioning tolerance. Particle drifts primarily cause global up-down asymmetries [10], which are beyond the scope of this work. Error fields originate from finite imperfections in coil manufacturing, installation misalignments, electromagnetic deformations, and ferromagnetic materials. In the standard magnetic configuration of W7-X, the boundary rotational transform ι at the plasma edge is close to unity. The boundary 5/5 island chain ($\iota = n/m = 5/5$, m, n for poloidal and toroidal mode number, respectively) is strongly affected by low-order resonant 1/1 and 2/2 error fields, while higher-order modes exert less influence on flux surface displacement and island width [6]. These error fields destroy stellarator symmetry, producing uneven power deposition across the ten divertor units and increasing the risk of localized overloading of plasma-facing components.

Five external trim coils [16] are designed to compensate intrinsic 1/1 error fields. Additionally, ten control coils [17], typically used to modify boundary island structure, can be employed to correct 2/2 error fields. Previous studies [6, 7] demonstrated effective mitigation of the 1/1 error field by adjusting the amplitude and phase of trim coil currents. This was verified through flux surface mapping [18] and thermocouple measurements on the test divertor units. Predictions for the amplitude and phase of the 2/2 error field, following successful 1/1 compensation, were derived by fitting flux surface mapping data [6].

In this study, divertor heat flux distributions across all units are utilized for error-field compensation. For the first time, control coils are employed to mitigate intrinsic 2/2 error fields using a carefully designed phase-scan experiment. The results demonstrate clear improvements in symmetry, comparable to those achieved in 1/1 error-field compensation with trim coils. This paper presents both the preparatory simulations for coil current waveforms and the results of phase-scan experiments.

2. Simulation preparation

2.1. Coil currents for error-field compensation

Previous compensations of the 1/1 error field employed amplitude and phase scans of trim coil currents based on cosine waveforms [7]. In this work, control coils are introduced for the first time to correct 2/2 error fields. A central question is determining the appropriate current settings in the control coils to generate the desired perturbation fields. To study the perturbation fields with different mode numbers, a change into

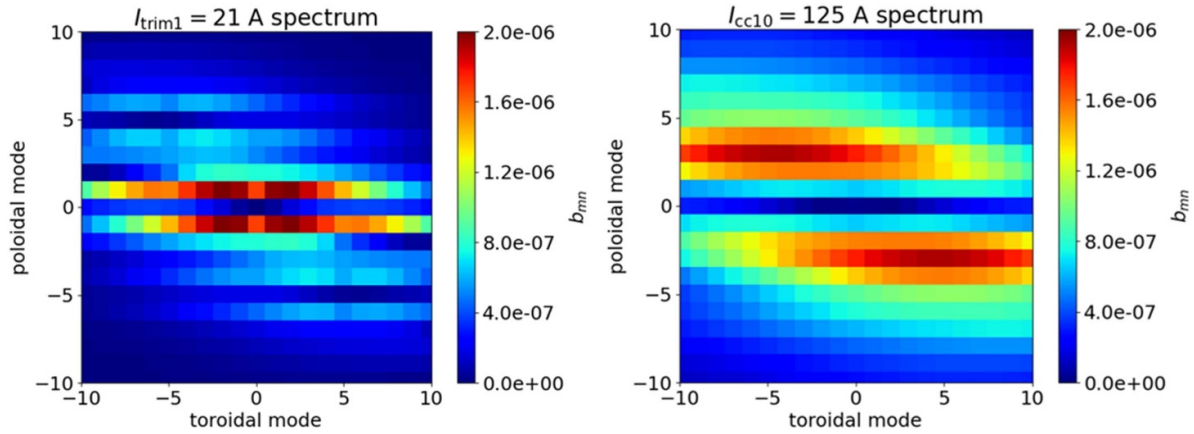

Figure 2. Power spectra of individual coils at the LCFS. The left panel shows results for a 21 A winding current in trim coil 1, while the right panel corresponds to a 125 A winding current in control coil 10.

the Fourier space domain is favorable. There are mainly three steps for this study.

1. Constructing flux coordinates for a flux surface in the vicinity inside the last closed flux surface (LCFS), and decomposing them into Fourier components [19]:

$$\{R,Z\} = \sum_{mn} \{R_{mn}, Z_{mn}\}\, \mathrm{e}^{\mathrm{i}(m\iota+sn)\varphi},$$
$$\varphi_{\mathrm{g}} = \varphi + \sum_{mn} \varphi_{mn} \mathrm{e}^{\mathrm{i}(m\iota+sn)\varphi}. \qquad (1)$$

   Here $s = 5$ is the W7-X modular symmetry, R, Z are major radius and vertical axis in cylindrical coordinate system. In figure 1, three flux coordinates are computed at the LCFS, where along a field line $\theta = \iota\varphi$ always holds (θ and φ are poloidal and toroidal angles). Their $\varphi = 0°$ planes, together with field lines traced from the outer mid-plane for one full toroidal turn inside the vessel are compared.
2. Calculating Fourier spectra for the perturbation fields produced by individual coils. The normalized normal mode b_{mn} of a perturbation field $\vec{B}_{\mathrm{pert}}$ is defined as the Fourier decomposition of the field component perpendicular to the flux surface in Boozer coordinate calculated in step (1) [6]:

$$b_{mn} = \frac{1}{rR_0B_0} \cdot \left(\vec{B}_{\mathrm{pert}} \cdot \left[\frac{\partial \vec{r}}{\partial \theta} \times \frac{\partial \vec{r}}{\partial \varphi} \right] \right)_{mn}, \qquad (2)$$

   where r is the minor radius of the flux surface, B_0 and R_0 are the average field and major radius on the magnetic axis, respectively. As an example, figure 2 shows the Fourier spectra at the LCFS generated by a 21 A winding current in trim coil 1 (trim1, located on the outboard side of module 1 with 48 windings) and a 125 A winding current in control coil 10 (cc10, positioned at half-module 10 with 8 windings). Because each coil occupies a specific toroidal angle in real space, the resulting toroidal modes are broadly distributed in Fourier space. The dominant poloidal mode numbers are 1 for trim1 and 2, 3, 4 for cc10, respectively.
3. Employing an optimization algorithm to determine current combinations that achieve target modes while suppressing unwanted harmonics. For the trim coils, for example, the targeted mode is set to $b_{11} = A \cdot \mathrm{e}^{\mathrm{i}\varphi_{\mathrm{g}}}$, while other dominant modes at $\iota = 1$ are constrained to zero. With the spectra of individual coils with unit currents obtained in the second step, the optimization effectively determines the optimal coil currents approaching the target modes as weighted combinations, given the linear superposition of their Fourier spectra. Specifically, the currents are obtained by minimizing a weighted sum of squared residuals between the target modes and the predicted modes from the linear superposition of the individual-coil spectra. The minimization is carried out using a quasi-Newton (BFGS) method with an analytically evaluated gradient [20]. Figure 3 presents the optimization results, where a mode amplitude of $A = 0.5 \times 10^{-4}$ and phase $\varphi_{\mathrm{g}} = 0°$ are prescribed for both the b_{11} and b_{22} fields using the five trim coils and ten control coils, respectively. Note that the amplitude of b_{11} is the sum of the $(1,-1)$ mode and its complex conjugate $(-1,1)$. While higher harmonics at $\iota = 1$ can be effectively suppressed, non-resonant sidebands (e.g. b_{14} in the trim coil case and b_{37} in the control coil case) remain unavoidable, though their influence on the boundary 5/5 island topology is expected to be minor. Furthermore, the optimized coil currents can be accurately fitted by a $\cos\varphi$ wave for the trim coils and a $\cos 2\varphi$ wave for the control coils, with negligible fitting errors when plotted against the toroidal center of the relevant coils. For instance, the central positions of cc10 and cc11 are at $-15°$ and $15°$, respectively.

A unique relationship is found between the phase shift of the cosine waveform describing the coil currents and the phase of the resulting perturbation field. This correlation enables straightforward preparation of phase-scan experiments for error-field compensation by sampling different phases of the coil current waveform. In these experiments, the phase of the perturbation field (b_{11} and b_{22}) is used as the reference

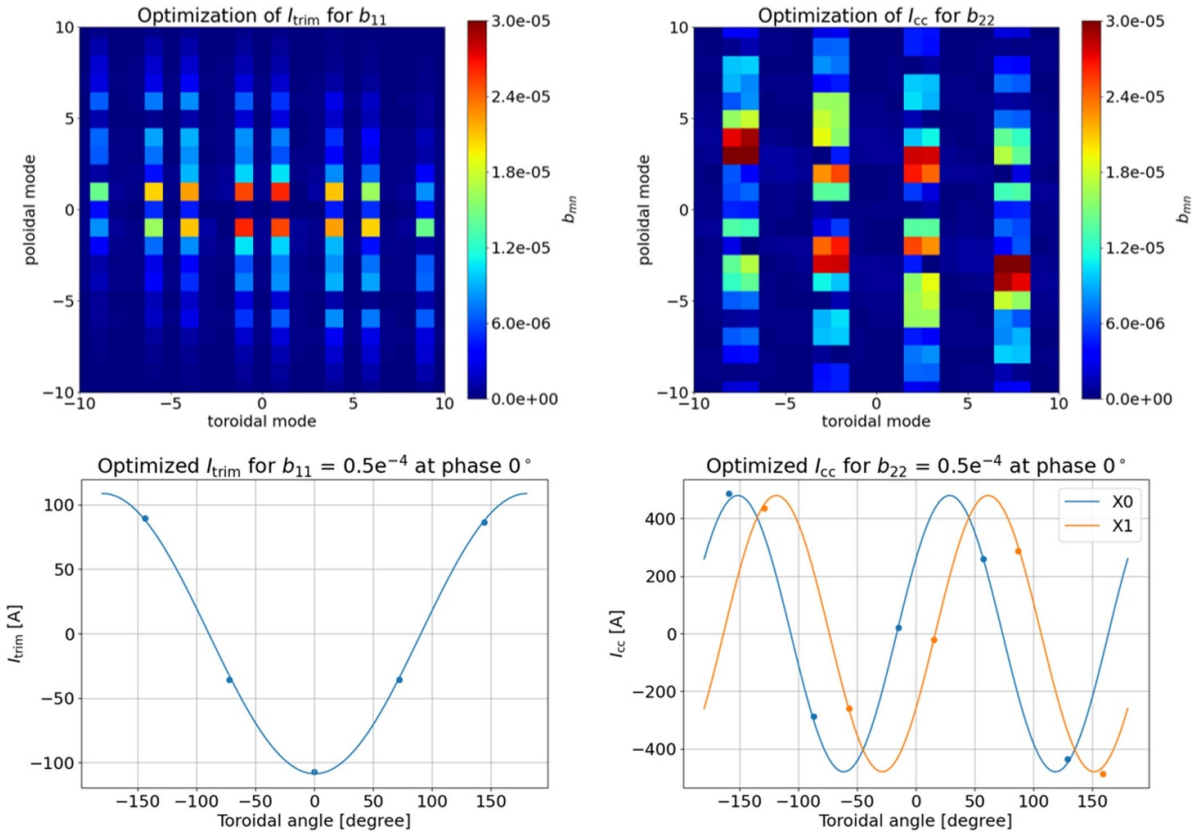

Figure 3. Optimized coil currents (lower panels) and the corresponding Fourier spectra (upper panels). The left column shows results for b_{11}, and the right column for b_{22}. In the coil current plots, dots represent the values obtained from the optimization function, while the curves indicate fits using simple cosine waveforms.

throughout the paper. A perturbation with phase of 0° has its maximal outward pointing field at the outboard side in the plane $\varphi_g = 0°$ in W7-X global coordinate, as previously defined in [6].

2.2. Perturbation field effect on divertor heat loads

To quickly estimate heat load distributions in the presence of external perturbation fields, the EMC3-Lite code [21] is employed. The code has been extensively benchmarked against experimental results under typical attached plasma conditions and has successfully reproduced the thermal footprints on the divertor target, particularly in the target-shadowed region [22]. This code simplifies the heat transport equation by considering only parallel electron heat conduction and perpendicular heat diffusion terms:

$$\nabla \cdot \left(-\kappa_e \nabla_{\parallel} T - \chi n \nabla_{\perp} T\right) = 0. \tag{3}$$

Here, it is assumed that the electron and ion temperatures are equal, i.e. $T = T_i = T_e$, and also for the density $n = n_i = n_e$ for the simulated hydrogen plasmas. The perpendicular heat diffusion coefficient is defined as $\chi = \chi_i + \chi_e$. At the target, the Bohm sheath boundary condition is applied within EMC3-Lite. In ideal simulations without external perturbation fields, the simulated target heat loads are identical across different target units.

Figure 4 presents the simulation results of integrated heat loads corresponding to the fitted coil currents shown in figure 3. Notably, the thermal loads on the targets can also be approximated using cosine functions, similar to the fitting performed for the coil currents. In the presence of a 1/1 perturbation field, the integral power distribution on the divertor targets can be expressed as:

$$P_i(\varphi_g) = a_{0,i} + A_{1,i}\cos(\varphi_g - \varphi_{1,i}), \quad i \in \{\text{up}, \text{low}\}. \tag{4}$$

Here, the integral power to the upper and lower targets is fitted separately. The toroidal angle $\varphi_g = 0°$ corresponds to the center of module 1 in the global coordinate system of W7-X and serves as the reference location for the two divertor units in this module (1 l and 1 u), as shown in figure 1. Accordingly, the toroidal angles of modules 2–5 are defined by $72°, 144°, -144°, -72°$, respectively. For a 2/2 perturbation, the power distribution is described by:

$$P_i(\varphi_g) = a_{0,i} + A_{2,i}\cos(2\varphi_g - \varphi_{2,i}). \tag{5}$$

Interestingly, when both the trim and control coils are applied simultaneously, the heat load distribution appears to be approximately superimposed and can be described by a combined function:

$$P_i(\varphi_g) = a_{0,i} + A_{1,i}\cos(\varphi_g - \varphi_{1,i}) + A_{2,i}\cos(2\varphi_g - \varphi_{2,i}). \tag{6}$$

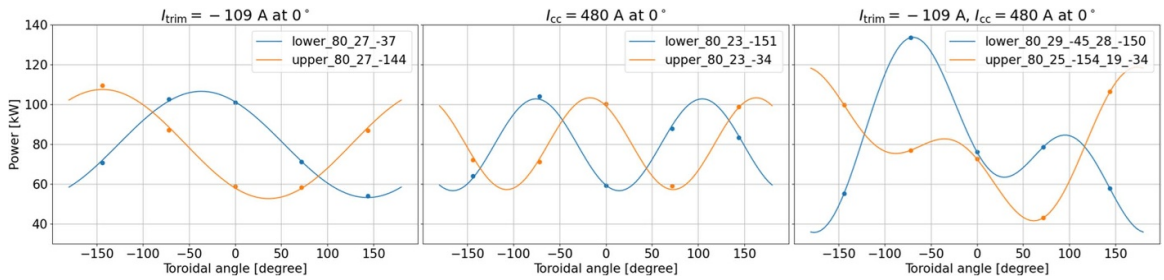

Figure 4. Simulated integrated power on five upper (orange) and five lower (blue) divertor units under specific trim coil currents (left) and control coil currents (middle), as shown in figure 3, as well as for the case of superimposed trim and control coil currents (right). The corresponding fitting coefficients are indicated in the legends of each panel, e.g. the legend '80_29_-45_28_-150' indicates the fitted values for a_0, A_1, φ_1, A_2, and φ_2, respectively from equation (6).

By comparing the fitted coefficients (shown in the figure legends) across all three cases, it is evident that the contributions from b_{11} and b_{22} can be partially disentangled from the integral target power. The fitting is not exact, particularly in the superimposed case, where overfitting is observed. This discrepancy may arise from sidebands, as illustrated in figure 3, which have minor effects on the edge topology.

The simulation results were obtained using a total input power of 800 kW, a separatrix electron temperature $T_e = 100$ eV, a density $n_e = 1 \times 10^{19}\,\mathrm{m}^{-3}$, and a perpendicular heat diffusion coefficient $\chi = 1\,\mathrm{m}^2\,\mathrm{s}^{-1}$. Increasing χ reduces the asymmetry across different target units due to the smoothing effect of diffusion. Conversely, when asymmetry is enhanced, either by a stronger perturbation field (e.g. mode amplitude $A > 1 \times 10^{-4}$) or by a significantly reduced $\chi < 0.1\,\mathrm{m}^2\,\mathrm{s}^{-1}$, the fitting procedure may fail, particularly if almost no power is deposited on certain divertor units.

Table 1. Phase-scan experiment performed on 20 240 918. Table includes program ID, amplitude of the coil current waveform, and the relevant phase of the produced b_{11} and b_{22} perturbation fields.

PID	I_{trim} (A)	$\varphi_{b_{11}}$ (°)	I_{cc} (A)	$\varphi_{b_{22}}$ (°)
31	−109	−162	0	0
32	−109	−162	0	0
33	−109	−126	0	0
34	−109	−90	0	0
35	−109	−54	0	0
36	−109	−18	0	0
41	−109	18	0	0
42	−109	54	0	0
50	−109	−18	480	126
51	−109	−18	480	54
54	−109	−18	480	126
57	−109	−18	480	−90
58	−109	−18	480	−18
59	−109	−18	480	90

3. Experimental results

3.1. Forward field

A phase-scan experiment comprising a sequence of discharges was performed at the beginning of the recent campaign to identify optimal coil settings for error-field compensation. Experiments were conducted in the standard magnetic configuration without planar coil currents, with 1.8 MW of electron cyclotron resonance heating and line-integrated density of $2 \times 10^{19}\,\mathrm{m}^{-2}$. Specific perturbation phases were generated using trim and control coil currents (as shown in table 1).

The relative standard deviation (Rstd) of the integrated power loads deposited onto the entire surface of a particular divertor unit P is calculated separately for the five upper and five lower targets. The average between $\mathrm{Rstd}_{\mathrm{up}}$ and $\mathrm{Rstd}_{\mathrm{low}}$ is then used to quantify the symmetry level for a given phase:

$$\mu_i = \frac{1}{5}\sum_{t=1}^{5} P_{t,i}, \quad i \in \{\mathrm{up}, \mathrm{low}\},$$
$$\mathrm{Rstd}_i = \frac{1}{\mu_i}\sqrt{\frac{1}{5}\sum_{t=1}^{5}(P_{t,i}-\mu_i)^2}, \quad \mathrm{Rstd} = \frac{1}{2}\sum_i \mathrm{Rstd}_i. \tag{7}$$

The amplitudes of the intrinsic b_{11} and b_{22} error fields are assumed to be approximately 0.5×10^{-4}, based on previous experimental results and simulation studies [6, 7]; therefore, no amplitude scans are conducted in this campaign. To generate a b_{11} field of this magnitude at the LCFS, a trim coil current amplitude of 109 A is required. Similarly, producing a b_{22} field of comparable strength requires 480 A for the control coils. See figure 3 for further details.

Figure 5 summarizes the results. A phase scan of b_{11} is performed first, showing that Rstd reaches a minimum near $\varphi_g = -18°$. And the closer the phase is to $-18°$, the better the heat load symmetry. This 'valley-shaped' profile of Rstd as a function of phase provides confidence in the phase-scan method and thermographic measurement for error-field compensation. The results indicate the presence of an intrinsic b_{11} field with a specific orientation, corresponding to the phase opposite to that of the optimal compensation field generated by the trim coils during the phase scans, i.e. at $\varphi_g = -18° + 180° = 162°$. It should be noted that two discharges are conducted at $\varphi = -162°$ for diagnostic purposes, which, as a byproduct, provide the error bars for the Rstd analysis. Together with an additional duplicate at $\varphi = 126°$ in the b_{22} phase scan (right subfigure), a global error bar of ∼0.03 is determined. This finite uncertainty may partly arise from the

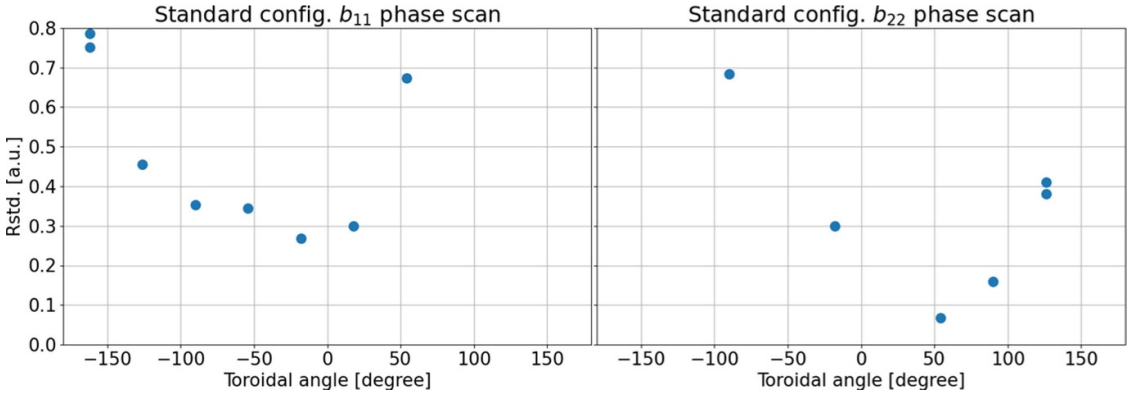

Figure 5. Experimental results of the Rstd of the integrated power on all divertor units for different phases of the perturbation field in the forward standard magnetic configuration. Left: Phase scan of the b_{11} field using trim coils. Right: Phase scan of the b_{22} field using control coils, with the optimal trim coil settings applied for b_{11} error-field compensation.

fact that these discharges are carried out at the beginning (commission phase) of the campaign, when control systems and the device are not yet fully stable (e.g. due to outgassing from the heated divertor), thereby affecting the surface temperature measurements obtained from the infrared cameras.

Building on the optimal trim coil settings, a phase scan of the control coils is performed to probe the phase of the remaining intrinsic b_{22} field. A 'valley' in Rstd is again observed, with a minimum at $\varphi_g = 54°$, indicating that the intrinsic b_{22} field has a phase of $\varphi_g = 54° - 180° = -126°$. While the minimum Rstd obtained with b_{11} error-field compensation saturates at approximately 0.27, it can be further reduced to 0.067 with the additional b_{22} error-field compensation. This confirms that the intrinsic b_{11} and b_{22} error fields are of similar magnitude, approximately 0.5×10^{-4}, as both are effectively compensated by the combined action of the trim and control coils, producing b_{11} and b_{22} fields of the same strength.

Figure 6 compares the measured temperature distributions for all 10 divertor units between the most asymmetric and symmetric cases. In the case with the largest Rstd, most heat load is concentrated on specific divertor units (e.g. 2 u and 4l), while units such as 1 l, 4 u, and 5l receive significantly less heat. With the optimal trim and control coil settings for error-field compensation, the heat loads are nearly uniform across all target units.

After correcting for optical distortion [23] and interpolating the measured thermal footprints from different infrared cameras onto a unified divertor grid [24], the heat flux can be calculated using the DELVER code [14]. Figure 7 presents three experimental results of the integrated power on the divertor: (a) the case with the largest Rstd ~ 0.75 ($I_{\mathrm{trim}} = -109$ A at $\varphi = -109°$) from the trim coil phase scans, (b) the case with optimal b_{11} error-field compensation, and (c) the case with both optimal b_{11} and b_{22} error-field compensations. The waveform in case (a) clearly exhibits a superposition of $\cos\varphi$ and $\cos 2\varphi$, as described in section 2.2, and can be fitted using the function $a_0 + a_1 \cos\varphi + a_2 \cos 2\varphi$, with fitting parameters shown in the legend. After correcting b_{11}, the fitted amplitude a_1 is strongly reduced, resulting in a waveform dominated by $\cos 2\varphi$ component, as shown in (b). Finally, in case (c), with both b_{11} and b_{22} fields compensated, the integral power waveform is nearly flat, indicating a highly symmetric heat load deposition across the machine modules.

In addition, as a confirmation of our experimental results, in (d) the divertor heat loads are simulated using EMC3-Lite, with an inverted sign for the best trim and control coil settings (mimicking intrinsic error fields) plus the trim coil setting in case (a). The simulated results are qualitatively consistent with the experimental results in the trend of the waveforms, although the asymmetry level is rather reduced. It should be noted that the same input parameters are used in the simulation as described in section 2.2, with the only modification being an increase in the total input power to 1.4 MW. Fine-tuning of these parameters may produce a better agreement with experiments, but it is not the aim of the present study. Additional factors which may cause mismatches between experiments and simulations include: other uncorrected side bands of the intrinsic error fields, harmonics introduced by the trim and control coils (as shown in 2.1.1), finite divertor misalignments, and the reduced heat transport physics in EMC3-Lite.

It is noteworthy that the successful compensation of both b_{11} and b_{22} error fields is largely attributable to the insights gained from previous studies [6, 7]. This validates the experimentally determined optimal trim coil settings used in the 2017 campaign with divertor thermocouples, despite the use of inertially cooled test divertor units at that time and a slight variation in the standard magnetic configuration—specifically, finite negative currents in the planar coils increasing the rotational transform compared to the present study [25]. In particular, $I_{\mathrm{Trim}} = 98$ A with $\phi_{\mathrm{Trim}} = 162°$, as listed in [7, table 1 therein], is equivalent in terms of the compensation-field direction to $I_{\mathrm{trim}} = -109$ A and $\varphi_{11} = -18°$ used in the present study. It should be noted that although the test divertor units used in 2017 and the present water-cooled divertor are nominally of identical geometry, small differences arising from manufacturing tolerances and alignment cannot be excluded. Despite the above mentioned different conditions between the earlier and present works, the conclusion on the compensation

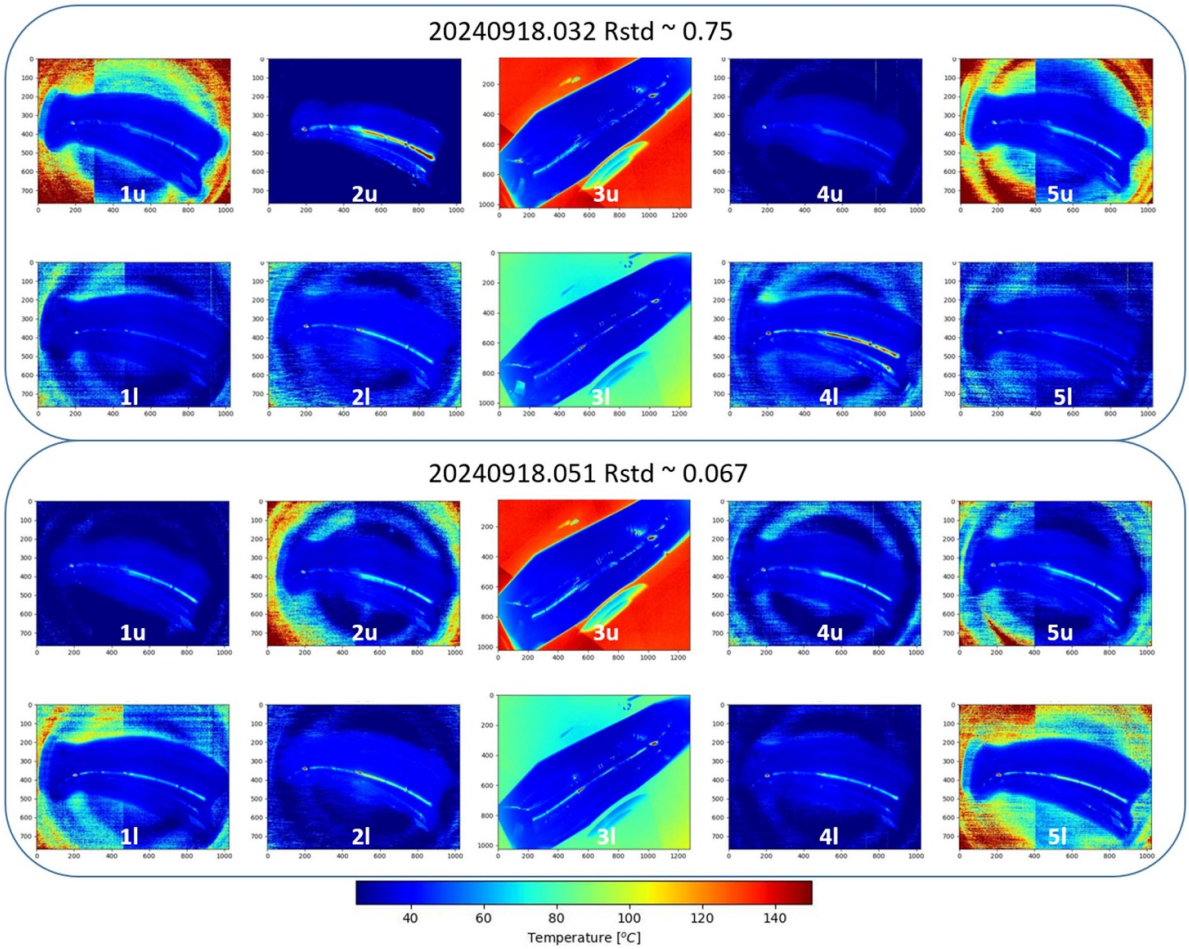

Figure 6. Measured temperature distributions across all 10 divertor units for the most asymmetric case (upper subfigure) with Rstd ∼0.75 and the most symmetric case (lower subfigure) with Rstd ∼0.067. The naming and location of divertor units are shown in figure 1.

field seems unchanged. These results suggest that both the magnetic coil systems and the intrinsic error fields have remained remarkably stable over approximately seven years. Furthermore, the findings provide good confirmation of the simulation predictions [6] for the phase and amplitude of the b_{22} error field, which were derived from fitting the flux surface mapping results following b_{11} error-field compensation in a narrow-mirror magnetic configuration with 5/5 boundary islands, similar to the standard configuration.

3.2. *Reversed field*

The reversed field configuration has been widely employed and plays an important role in studying drift effects in fusion devices, including W7-X [10]. However, the results of error-field compensation in the reversed field have not yet been systematically reported. This is partly due to the limited number of pulses available from earlier phase-scan experiments in the reversed configuration, and partly due to the complexity in interpreting the results. In previous experiments, no optimal compensation phase was identified in the reversed field. Neither identical trim-coil settings nor settings with flipped currents as used in the forward field led to a noticeable improvement in divertor temperature symmetry measured from thermocouples [7].

A reversed field configuration in W7-X can be achieved by reversing the polarity of the currents in all main coils (non-planar and planar coils). This produces the same magnetic topology (i.e. the spatial geometry of the magnetic field structure) as in the corresponding forward field, but with the magnetic field direction reversed along any given field line. The main toroidal field B_{tor} points clockwise when viewed from above in the reversed configuration, opposite to the direction shown in figure 1.

In the previous campaign, we proposed dedicated phase-scan experiments in the reversed standard magnetic configuration, using plasma parameters and perturbation strengths identical to those in the forward field, i.e. −109 A as the amplitude for the trim coil waveform, and 480 A for the control coil. First, a sequence of phase-scan discharges was carried out using trim coils to determine the optimal phase for correcting the b_{11} error field. Subsequently, using the best trim-coil setting, control-coil phase-scan discharges were performed to correct the b_{22} component. The complete pulse list is provided in table 2. Discharge 20 250 218.048, which was operated without trim or control coil currents, serves as a reference. Compared with the forward field study, a larger number

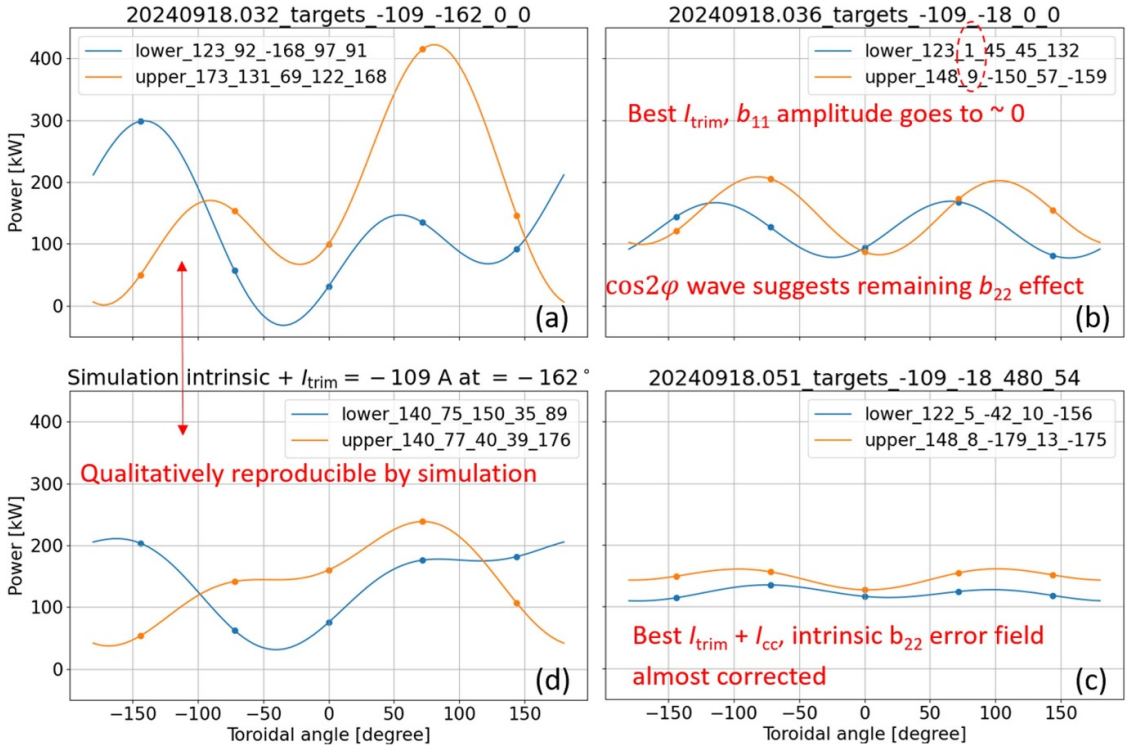

Figure 7. Waveform of integral power on divertor units. (*a*) Experimental result from 20 240 918.032 with $I_{\rm trim} = -109A$ at $\varphi = -162°$. (*b*) Result with the optimal trim coil setting in 20 240 918.036. (*c*) Result with both optimal trim and control coil settings in 20 240 918.051. (*d*) Simulated result with the derived intrinsic error field plus the trim coil setting used in (*a*). The legend shows the fitting coefficients of the respective waveform as described in figure 4.

Table 2. Phase-scan experiment performed on 20 250 218 in reversed field. Table includes program ID, amplitude of the coil current waveform, and the relevant phase of the produced b_{11} and b_{22} perturbation fields.

PID	$I_{\rm trim}$ (A)	$\varphi_{b_{11}}$ (°)	I_{cc} (A)	$\varphi_{b_{22}}$ (°)
48	0	0	0	0
49	−109	18	0	0
54	−109	54	0	0
55	−109	90	0	0
56	−109	126	0	0
58	−109	162	0	0
59	−109	−162	0	0
60	−109	−126	0	0
61	−109	−90	0	0
62	−109	−54	0	0
63	−109	−18	0	0
64	−109	126	480	−162
65	−109	126	480	−126
66	−109	126	480	−90
67	−109	126	480	−54
68	−109	126	480	−18
69	−109	126	480	18
70	−109	126	480	54
71	−109	126	480	90
72	−109	126	480	126
73	−109	126	480	162

of discharges were requested and executed due to the limited understanding of error fields in the reversed configuration from previous experiments.

Figure 8 presents the Rstd results for the b_{11} (left) and b_{22} (right) phase scans. Notably, the trim coils do not produce a clear improvement in symmetry. The minimum Rstd occurs at

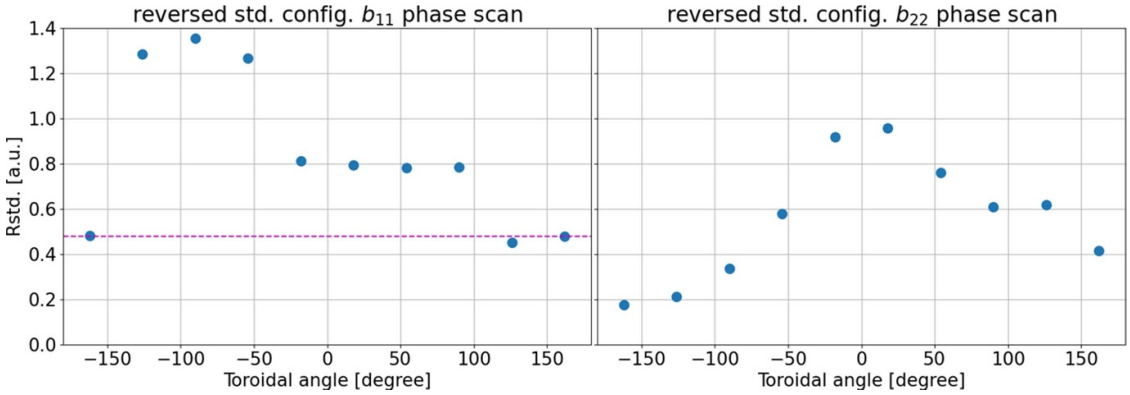

Figure 8. Experimental results of the Rstd of the integrated power on all divertor units for different phases of the perturbation field in the reversed standard magnetic configuration. Left: Phase scan of the b_{11} field using trim coils. A horizontal purple dashed line indicates the Rstd value for the reference discharge without any trim and control coil currents. Right: Phase scan of the b_{22} field using control coils, with the optimal trim coil settings applied for b_{11} error-field compensation.

$\varphi_g = 126°$ among the ten uniformly sampled phases, yielding a value of approximately 0.45, which is close to that of the reference discharge, about 0.48. Moreover, unlike the forward-field case, no pronounced Rstd minimum ('valley') is observed in the b_{11} phase-scan results. Instead, the Rstd values cluster into three distinct levels: a high level of about 1.3 from $-126°$ to $-54°$, a medium level of about 0.8 from $-18°$ to 90°, and a low level comparable to the reference ($\sim$0.48) from 126° to 198° (198° being equivalent to $-162°$).

Figure 8(right) shows the b_{22} phase-scan results obtained on top of the best trim coil setting. In contrast to the b_{11} scan, a clear Rstd minimum ('valley') is observed. The minimum Rstd appears at $\varphi_g = -162°$ with a value of approximately 0.18, while the maximum, Rstd $\sim$0.96, occurs at 18°, i.e. in the direction opposite to the optimal compensation b_{22} field generated by the control coils. The pronounced difference in Rstd between opposite phases confirms the compensation of the intrinsic b_{22} error field, whose amplitude is about $\sim 0.5 \times 10^{-4}$ and whose phase is approximately 18°.

Figure 9 presents detailed experimental integral power distributions for four representative discharges: (a) the reference case without any compensation field; (b) the case with the largest Rstd value of approximately 1.36, obtained with $I_{\text{trim}} = -109$ A at $\varphi = -90°$; (c) the case with the minimum Rstd achieved using both trim and control coil currents; and (d) the case with the best trim coil setting. The waveforms in (a) and (d) are very similar, confirming that the trim coils provide only marginal improvement in symmetry relative to the reference case, consistent with figure 8(left). The fitting parameters of the waveforms, shown in the legends, indicate a relatively low intrinsic b_{11} error field ($A_1 < 40$ in (a) and $A_1 < 30$ in (d)), while the b_{22} amplitude exceeds b_{11} by at least a factor of two. In the most asymmetric case, shown in (b), most of the heat load is deposited on divertor units 5 u and 1 l, each receiving more than 500 KW, whereas the remaining units each receive, on average, about 50 KW. Finally, a rather symmetric heat load distribution is achieved in (c), primarily as a result of the compensation of the b_{22} field by the control coils, although the optimal trim coil setting is also applied.

3.3. Summary and discussion

The optimal settings for error-field compensation using trim and control coils are summarized in table 3 for both the forward and reversed standard magnetic configurations. The main conclusions can be summarized as follows:

- Pronounced intrinsic b_{22} error fields are present and have been effectively mitigated using the control coils. With the application of the control coils, the value of Rstd is reduced by approximately 75% in the forward field and by 60% in the reversed field relative to the cases with trim coils only.
- Error-field compensation is less effective in the reversed configuration than in the forward configuration. The minimum Rstd achieved using both trim and control coils in the reversed field is larger by a factor of 2.7 compared with that obtained in the forward field.
- The optimal compensation phase and amplitude for the b_{11} component in the forward-field configuration are in good agreement with the values reported in [7]. Considering differences in diagnostics, divertor components, and slightly modified magnetic configurations, the close agreement between the earlier and present results is notable and encouraging.
- For both b_{11} and b_{22} compensations, a phase difference of approximately 144° is observed between the forward and reversed field configurations. However, in the reversed-field b_{11} phase scan, a phase interval of about 72° yields similarly low Rstd values, rather than a single well-defined minimum.

Several points require further discussion:

1. The reason why the b_{11} phase-scan experiment in the reversed field does not produce a clear improvement in symmetry relative to the reference discharge remains unclear. Instead of a distinct minimum forming a 'valley-like' profile in Rstd, three separate levels of Rstd are observed, depending on the phase range.

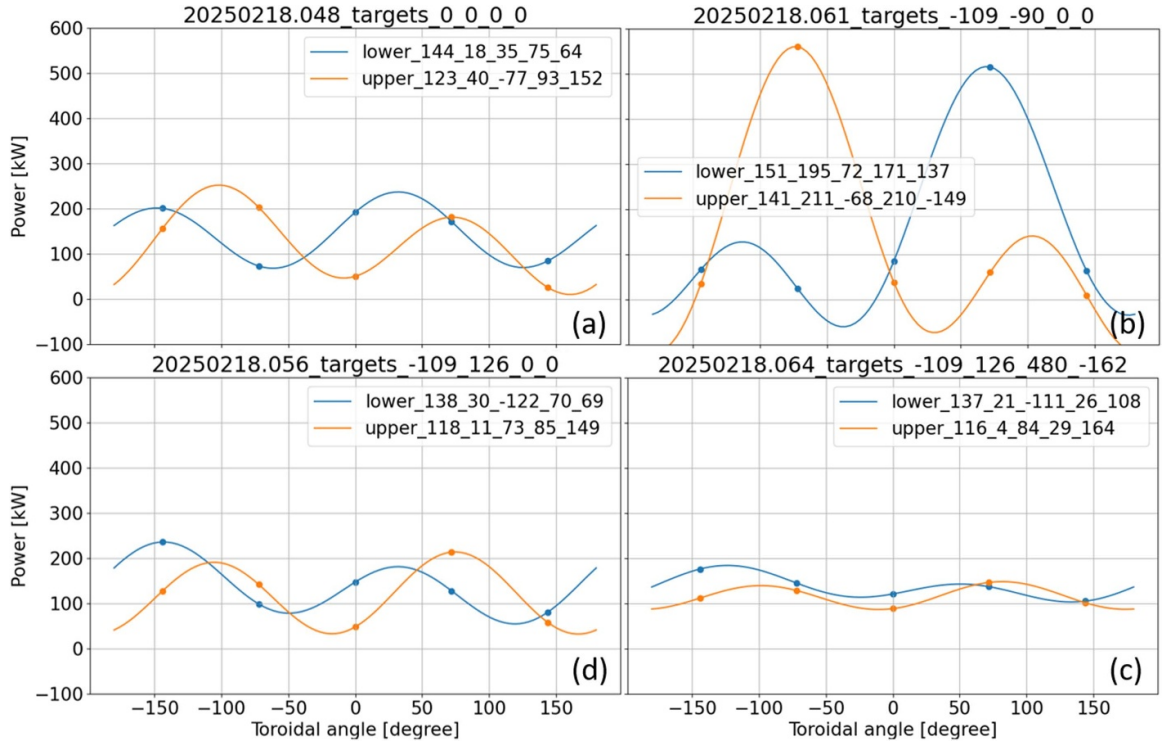

Figure 9. Waveform of integral power on divertor units in reversed field. (*a*) Reference result from 20 250 218.048 without any trim or control coil currents. (*b*) 20 250 218.061 with the highest Rstd value. (*c*) Result with both the optimal trim and control coil settings in 20 250 218.064. (*d*) Result with only the optimal trim coil setting in 20 250 218.056 without control coils. The legend shows the fitting coefficients of the respective waveform as described in figure 4.

Table 3. Optimal coil settings for error-field compensation in forward and reversed standard magnetic configurations. Table includes program ID, amplitude of the coil current waveform, the relevant phase of the produced b_{11} and b_{22} perturbation fields, and the minimum Rstd reached for the trim coil only case ($\mathrm{Rstd_{trim}}$) and for using both the trim and control coil case ($\mathrm{Rstd_{trim+cc}}$).

PID	I_{trim} (A)	$\varphi_{b_{11}}$ (°)	I_{cc} (A)	$\varphi_{b_{22}}$ (°)	$\mathrm{Rstd_{trim}}$	$\mathrm{Rstd_{trim+cc}}$
20 240 918.051 (forward)	−109	−18	480	54	0.27	0.067
20 250 218.064 (reversed)	−109	126	480	−162	0.45	0.18

2. In the forward-field b_{11} phase-scan experiment, the intended reference discharge was compromised due to dropped gyrotrons and the absence of one infrared camera measurement; consequently, it was not included in the present analysis. Nevertheless, previous work demonstrated a clear improvement in divertor load symmetry in the forward field when trim coils were applied, compared with a reference discharge (see figures 11 and 8 in [7]). This contrasts with the behavior observed for the reversed-field configuration in the present study.
3. Although a phase difference of approximately 144° between the forward and reversed configurations is identified, the optimal phase for reversed-field b_{11} compensation lies within a relatively broad range from 126° to 198°. Similarly, for reversed-field b_{22} compensation, the difference in Rstd between −162° and −126° is small. These observations indicate that the direction of the compensation fields for both b_{11} and b_{22} is nearly opposite between the forward and reversed configurations. This is consistent with the interpretation that the dominant error fields originate primarily from the magnetic coils themselves, e.g. due to manufacturing tolerances, installation misalignments, or electromagnetic deformations. In the case of electromagnetic deformation, it is noteworthy that although the forces and resulting deformations are identical in forward and reversed fields, the induced error fields have opposite directions due to the reversal of current polarity.
4. The amplitudes of the coil current waveforms (I_{trim} and I_{cc}) were predefined to generate b_{11} and b_{22} perturbations with a mode amplitude of 0.5×10^{-4}, based on earlier results and predictions [6, 7]. The optimal phases were determined from phase-scan experiments with a sampling interval of 36°. Further fine-tuning of both amplitude and phase could potentially yield additional improvements, but only to a limited extent. Owing to the strong suppression of the cosine waves, an almost uniform heat-load distribution across machine modules has been achieved.
5. Additional limitations remain in achieving perfect symmetry. Higher harmonics present in the intrinsic error fields cannot be compensated by the existing coil systems. Furthermore, additional sidebands produced by the trim and control coils are unavoidable, as shown in figure 3.

Additional variations may arise from differences in divertor alignment as well as measurement uncertainties of thermography across divertor units. However, these effects are expected to have only a minor influence on the mitigation of the dominant intrinsic error-field components, namely the b_{11} and b_{22} modes.

4. Conclusion

Divertor heat loads, calculated from the measured surface temperatures of all ten divertor units using infrared cameras, are employed to support a quantitative study of intrinsic error fields in W7-X. For the first time, in addition to the b_{11} error-field compensation using trim coils, the intrinsic b_{22} error field is compensated by symmetrizing the divertor integrated power through a phase-scan experiment employing control coils. The design of experiments was guided by comprehensive simulations, which established a direct link between coil current waveforms and the resulting perturbation fields. Furthermore, simulations of divertor heat loads under perturbation fields indicate that the typical heat load distribution can be represented as a superposition of cosine functions. With the b_{22} error field compensated, a significant improvement in the symmetry of heat loads is achieved—an enhancement that cannot be realized with trim coils alone. The experimental results also support previous findings [7] regarding the phase and amplitude of the b_{11} error field in the forward field obtained during the first divertor campaign, suggesting that the magnetic coil systems have maintained reliable and rigid mechanical integrity over the past seven years. Additionally, the newly achieved b_{22} error-field compensation confirms the simulation predictions [6] from flux surface mapping results. First systematic investigation of error-field compensation in the reversed magnetic configuration has been conducted. Although the application of trim coils alone does not lead to a clear improvement in target symmetry (for which the reason is not clear), a substantial improvement is achieved through the successful compensation of the intrinsic b_{22} error field using control coils. The compensation field is found to have nearly opposite directions in the forward and reversed configurations, which supports the interpretation that the intrinsic error field predominantly originates from the main coil system itself.

Acknowledgment

This work has been carried out within the framework of the EUROfusion Consortium, funded by the European Union via the Euratom Research and Training Programme (Grant Agreement No. 101052200 — EUROfusion). Views and opinions expressed are however those of the author(s) only and do not necessarily reflect those of the European Union or the European Commission. Neither the European Union nor the European Commission can be held responsible for them.

ORCID iDs

Yu Gao 0000-0001-8576-0970
Sergey Bozhenkov 0000-0003-4289-3532
Yuhe Feng 0000-0002-3846-4279
Sebastian Thiede 0009-0007-8018-8187
Marcin W. Jakubowski 0000-0002-6557-3497
Joachim Geiger 0000-0003-4268-7480
Torsten Stange 0000-0003-4154-1455
Olaf Grulke 0000-0001-7879-8671
Michael Endler 0000-0003-2314-8393
Matthias Otte 0000-0003-3134-7579
Dirk Naujoks 0000-0003-4265-6078
Joris Fellinger 0000-0003-2380-0329
Fabio Pisano 0000-0003-0162-0562

References

[1] Pedersen T.S. *et al* 2018 First results from divertor operation in Wendelstein 7-X *Plasma Phys. Control. Fusion* **61** 014035
[2] Klinger T. *et al* 2019 Overview of first Wendelstein 7-X high-performance operation *Nucl. Fusion* **59** 112004
[3] Wolf R.C. *et al* 2019 Performance of Wendelstein 7-X stellarator plasmas during the first divertor operation phase *Phys. Plasmas* **26** 082504
[4] Grulke O. *et al* 2024 Overview of the first Wendelstein 7-X long pulse campaign with fully water-cooled plasma facing components *Nucl. Fusion* **64** 112002
[5] Geiger J., Beidler C.D., Feng Y., Maaßberg H., Marushchenko N.B. and Turkin Y. 2014 Physics in the magnetic configuration space of W7-X *Plasma Phys. Control. Fusion* **57** 014004
[6] Bozhenkov S., Otte M., Biedermann C., Jakubowski M., Lazerson S.A., Sunn Pedersen T. and Wolf R.C. 2018 Measurements and correction of the 1/1 error field in Wendelstein 7-X *Nucl. Fusion* **59** 026004
[7] Lazerson S.A. *et al* 2018 Error fields in the Wendelstein 7-X stellarator *Plasma Phys. Control. Fusion* **60** 124002
[8] Gao Y. *et al* 2019 Effects of toroidal plasma current on divertor power depositions on Wendelstein 7-X *Nucl. Fusion* **59** 106015
[9] Gao Y. *et al* 2024 Heat and particle exhaust in high-performance plasmas in Wendelstein 7-X *Nucl. Fusion* **64** 076060
[10] Hammond K.C. *et al* 2019 Drift effects on W7-X divertor heat and particle fluxes *Plasma Phys. Control. Fusion* **61** 125001
[11] Gao Y. *et al* 2020 Understanding baffle overloads observed in high-mirror configuration on Wendelstein 7-X *Nucl. Fusion* **60** 096012
[12] Jakubowski M. *et al* 2018 Infrared imaging systems for wall protection in the W7-X stellarator (invited) *Rev. Sci. Instrum.* **89** 10E116
[13] Fellinger J., Lippmann U., Greve H., Alhashimi M., Schülke M., Äkaslompolo S., Drewelow P., Jakubowski M., König R. and Lorenz A. 2020 Design of endoscopes for monitoring water-cooled divertor in W7-X *Fusion Eng. Des.* **158** 111841
[14] Thiede S. *et al* 2026 Improving heat flux calculations for the non-axisymmetric loads on plasma facing components in Wendelstein 7-X with DELVER *Rev. Sci. Instrum.* **97** 043504
[15] Herrmann A. 2001 Limitations for divertor heat flux calculations of fast events in tokamaks *28th EPS Conf. on Controlled Fusion and Plasma Physics* (*Madeira, Portugal, 18–21 June 2021*) (European Physical Society) pp 2109–12

(available at: https://lac913.epfl.ch/epsppd3/2001/html/authors/nav/AutH02fr.html)
[16] Rummel T., Risze K., Kiszlinger J., Koppen M., Fullenbach F., Neilson H., Brown T. and Ramakrishnan S. 2012 The trim coils for the Wendelstein 7-X Magnet System *IEEE Trans. Appl. Supercond.* **22** 4201704
[17] Füllenbach F. *et al* 2020 Commissioning of the Wendelstein 7-X in vessel control coils *IEEE Trans. Plasma Sci.* **48** 2635
[18] Otte M. *et al* 2016 Setup and initial results from the magnetic flux surface diagnostics at Wendelstein 7-X *Plasma Phys. Control. Fusion* **58** 064003
[19] Bozhenkov S., Geiger J., Grahl M., Kißlinger J., Werner A. and Wolf R.C. 2013 Service oriented architecture for scientific analysis at W7-X. An example of a field line tracer *Fusion Eng. Des.* **88** 2997
[20] Shanno D.F. 1970 Conditioning of quasi-Newton methods for function minimization *Math. Comput.* **24** 647
[21] Feng Y. (W7-X Team) 2022 Review of magnetic islands from the divertor perspective and a simplified heat transport model for the island divertor *Plasma Phys. Control. Fusion* **64** 125012
[22] Gao Y. *et al* 2023 Improvement in the simulation tools for heat distribution predictions and control of baffle and middle divertor loads in Wendelstein 7-X *Nucl. Fusion* **63** 026031
[23] Pisano F. *et al* 2020 Tools for image analysis and first wall protection at W7-X *Fusion Sci. Technol.* **76** 933
[24] Gao Y., Jakubowski M.W., Drewelow P., Pisano F., Puig Sitjes A., Niemann H., Ali A. and Cannas B. 2019 Methods for quantitative study of divertor heat loads on W7-X *Nucl. Fusion* **59** 066007
[25] Lazerson S.A. *et al* 2019 Tuning of the rotational transform in Wendelstein 7-X *Nucl. Fusion* **59** 126004